Determination of Shallow Water Depths using Inverse Probability Weighted Interpolation: A Hybrid System-Based Method

Salah, M.
Department of Surveying Engineering, Faculty of Engineering Shoubra - Benha University , 108 Shoubra st., Cairo – Egypt, E-mail: engmod2000@yahoo.com

Abstract
A method for the determination of bathymetry from the new and freely available 11-band Landsat-8 multispectral satellite imagery and sample depth measurements has been proposed. The method starts with a few reference points, where both reflectance and water depths are known. Several preprocessing operations were done before depth estimation. First, the image was geometrically and atmospherically corrected and then segmented into land and water. Second, Lansat-8 blue band was converted to reflectance. Third, two different algorithms were used to assign each pixel to each of the reference points. The algorithms used include: Naïve Bayesian (NB) as a statistical model; and Multilayer Perceptron (MLP) as a neural network model, which offer complementary information. Outputs are probability images corresponding to each known depth. In order to achieve a robust decision about the obtained probabilities, the Fuzzy Majority Voting (VMV) algorithm was then applied for combining measures of probability from the two algorithms. Finally, the water depths were derived from the combined probabilities based on an inverse probability weighted interpolation technique (IPWI). The proposed method enabled the retrieval of water depths of less than 5 m at a relatively high level of accuracy, 0.19 m. However, accuracy further decreases for the water depths of more than 10 m.

1. Introduction

Estimation of water depths plays an important role in monitoring water level for solving a wide variety of engineering problems. Currently, bathymetric data are acquired based on single- or multi-beam echo-sounding and airborne Light Detection and Ranging (LiDAR). The field data collection at a site is expensive and time consuming and sometimes extremely difficult in shallow water regions since the data tend to be extrapolated (Kao et al., 2009). Satellite data can be an attractive method for determining shallow water depths due to difficulties using traditional methods (Stumpf et al., 2003). The digital images acquired by the remote sensing satellites consist of the solar reflectance from the earth's surface which is modified by atmospheric constituents. The basic concept of using optical satellite imagery to determine shallow water depths depends on the ability of visible light to penetrate water, reach the seafloor and then reflect back to the sensor. Recently, a variety of optical satellites were lunched with higher spatial and radiometric resolution and used for estimating water depths. For instance: SPOT (Kao et al., 2009 and Mohamed et al., 2015); IRS-1C/1D LISS-III (Pattanaik et al., 2015); IKONOS (Stumpf et al., 2003 and Abileah, 2006); WorldView-2 (Loomis, 2009, Puetz et al., 2009, Bramante et al., 2010, Lee et al., 2011, Doxania et al., 2012, Mallick et al., 2014 and Yuzugullu and Aksoy, 2014); RapidEye (Monteys et al., 2015) and Landsat TM (Mgengel and Spitzer, 1991, Bierwirth et al., 1993, Jiazhu and Yuming, 2002, Fuxing and Qian, 2003 and Hoepffner and Zibordi, 2009). In Hoepffner and Zibordi, 2009), the blue band of the Landsat TM has proved to be invaluable in estimating bathymetry because of its greater depth penetration. The new and freely available 11-band Landsat-8 multispectral satellite imagery has proved to be invaluable in estimating bathymetry because of its greater depth penetration. Pacheco et al., (2015) applied a linear transform algorithm to estimate water depths of the near shore from Landsat-8 imagery. The algorithm was tuned with available bathymetric LiDAR data. The results showed a root mean square error (RMSE) of 0.89 m for depths of up to 12 m. Tang and Pradhan (2015) have applied the ratio transform proposed by Stumpf et al., (2003) to extract bathymetric information from Landsat-8 satellite imagery. The average uncertainties obtained was 1.52 m, with a highest RMSE of 3.76 m, and lowest RMSE of 0.02 m. The correlation coefficient between the estimated and endorsed bathymetry depths was 0.9054.

Several approaches have been applied for estimating bathymetry from satellite imagery including: the Wave Kinematics Bathymetry (WKB) (Piotrowski and Dugan, 2002); the standard linear transform and the new ratio transform algorithms (Stumpf et al., 2003); look-up table and ratio classifications (Louchard et al., 2003); Linear Band Model (Lyzenga et al., 2006); A least-squares-fit (Lee et al., 2011); local maximum likelihood (ML) (Jay and Guillaume, 2014). These algorithms perform under the assumption that water properties such as attenuation and quality are the same for a given area (Su et al., 2008); this may lower depth accuracy if this assumption is not achieved. On the other hand, linear techniques such as interpolation and least-squares regression result in poor bathymetry estimation because of the system's nonlinear dynamics (Roehl and Conrads, 2006). In recent years, artificial neural networks (ANNs) have been used for water depth estimation. An ANN model is a flexible mathematical structure capable of describing complex nonlinear relations between input and output datasets. While there are numerous ANN architectures that have been studied by researchers (Juanita and Ronald, 1998, Roehl and Conrads, 2006 and Ceyhun and Yalçın, 2010), the most commonly used type is the *MLP* (Rumelhart et al., 1986). It has been applied successfully for estimating water depths from optical satellite imagery (Mehdi et al., 2013 and Mohamed et al., 2015). The objective of this contribution is to compensate for the major weaknesses of the majority of existing models which require a complex estimation for a number of water column parameters such as bottom type; attenuation coefficients; and water quality. This can be achieved by combining measures of probability from the *MLP* and *NB* models, which offer complementary information, and hence the obtained depths can be improved. This paper is organized as follows. Section 2 describes the study area and data sources. Section 3 describes the experiments while Section 4 presents and evaluates the results. We summarize our results in Section 5.

2. Study Area and Data Sources

The study site is selected at Al Guna, located 25 kilometers north of Hurghada on the west coast of the Red Sea as shown in figure 1. Hurghada is a city in the Red Sea Governorate of Egypt. It is a major tourist center and the third largest city in Egypt located on the Red Sea coast, after Suez and Ismailia. The area was selected because: 1) it is characterized by shallow and clear waters; 2) detailed bathymetric data are available; 3) there is a variation of water depths. The test area covers approximately 7 x 7 km and lies between latitudes 27°21′43″ and 27°25′30″ N and longitudes 33°39′03″ and 33°43′28″E.

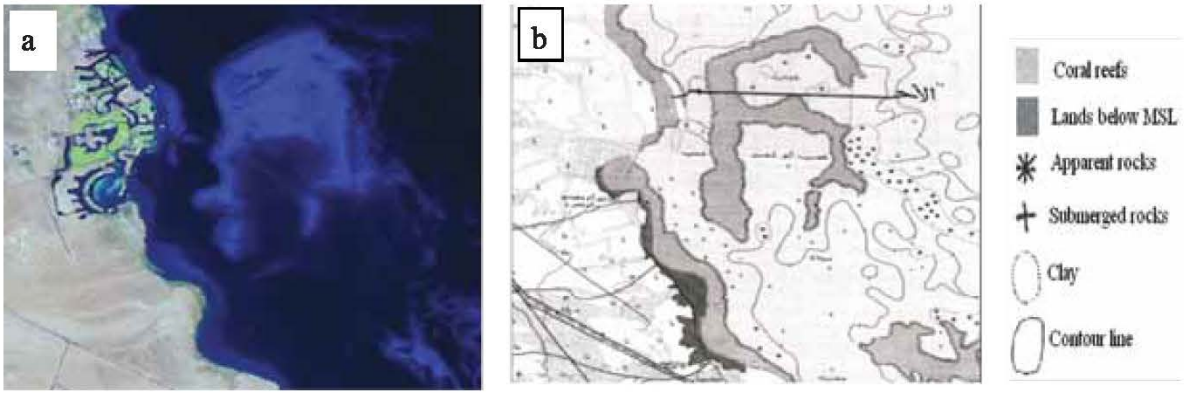

Figure 1: a) Landsat-8 satellite image; b) ESA 1:50,000 underwater topographic map

Table 1: Characteristics of Echo-sounder and RTK–DGPS

Sounding	Echotrac CV 100
Frequency	200 kHz
Positioning (RTK–DGPS)	Trimble R6/5800
Resolution	25 m
Echo-sounding accuracy	0.01 m ±0.1% of depth
HL accuracy of RTK positioning	8 mm + 1 ppm RMS
VL accuracy of RTK positioning	15 mm + 1 ppm RMS

The characteristics of the available datasets are as follow:

a) The Landsat image was collected on 21April 2015 as shown in figure 1. Landsat-8 is a new satellite imaging platform launched in early 2013 acquiring panchromatic images with 15 m resolution and multispectral images with 30 m resolution at nadir. The bands include: Band 1 – coastal aerosol (430 - 450 nm); Band 2 – blue (450 - 510 nm); Band 3 – green (530– 590 nm); Band 4 – red (640– 670 nm); Band 5 - Near Infrared (NIR) (880– 850 nm); Band 6 - Short-wave Infrared (SWIR) 1(1570– 1650 nm); Band 7 - Short-wave Infrared (SWIR) 2 (2110– 2290 nm); Band 8 – Panchromatic (500– 680 nm); Band 9 – Cirrus (1360– 1380 nm); Band 10 – TIRS 1 (10600 – 11190 nm); Band 11 – TIRS 2 (11500– 12510 nm). As can be observed, the image has been acquired in optimal conditions, in terms of clear sky and clear water. The visibility of the bottom topography is much better with blue band which allows a penetration of up to 20 m. The lighter the blue color in the image, the shallower the water.

b) A 1:50,000 underwater topographic map, as shown in figure 1b, over the same area was produced in 1971 from aerial photographs of scale 1:25,000 and last updated in 1990. The map is published by the Egyptian Survey Authority (ESA), projected on the WGS 84 / UTM zone 36N. The depth in this area according to the maps is ranging from 2 m to 25 m; the average water depth is 5.5 m.

The echo-sounding bathymetries in the study area were measured in November 2011, with survey positions being referenced to the UTM/WGS84 zone 36N and already reduced to tidal datum. The total number of depth observations taken was 1158. Table 1 summarizes the characteristics of the used Echo-sounder and RTK–DGPS. It is worth noting that for the test area, the water bottom is stable and there are no major currents that can affect the water depths. Because of that, the comparison assumes that there had been no significant change in the bathymetry in the four-year interval between field surveying and image acquisition dates.

3. Methodology

The proposed method is composed of several key steps as shown in figure 2. The main procedures are fully discussed in the following sections.

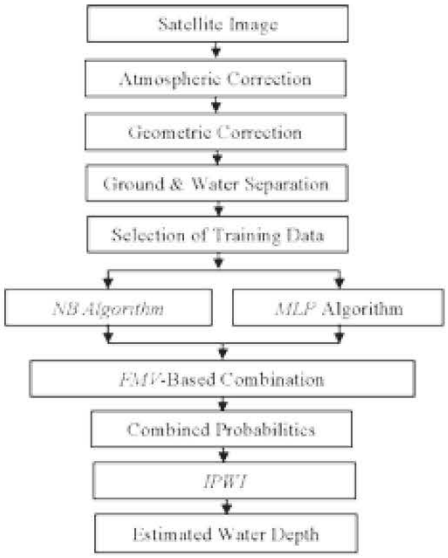

Figure 2: Determination of shallow water depths using *IPWI*

3.1 Atmospheric Correction of Landsat-8 Data

Atmospheric corrections accounted for surface reflection and sky radiance. The atmospheric absorption and scattering can weaken the solar radiation energy during the satellite imaging, which greatly influences the information extraction process, so the remote sensing imagery must be atmospherically corrected. For Landsat-8, the number of steps necessary in the atmospheric correction process can be reduced when compared with previous Landsat missions because terms have been embedded in Landsat-8 DN values (Keith et al., 2014):

3.1.1 Conversion to radiance

Landsat-8 data are provided as digital number (DN) images, the first step is to calibrate to radiance, which is the amount of energy received by the sensor per second (W) per steradian (sr) per cubic meter (m^3). This is written as $Wsr^{-1}m^{-3}$ or $Wsr^{-1}m^{-3}nm^{-1}$ for a given wavelength (nm) (NASA, 2011). For Landsat-8, a linear equation is used to convert from DN to radiance (L):

$$L = (DN * G) + I \qquad \text{Equation 1}$$

The gain (G) and intercept (I) are different for each band and are provided in the Landsat-8 header file.

3.1.2 Top of atmosphere (TOA) reflectance

For relatively clear Landsat-8 scenes, a reduction in between-scene variability can be achieved by converting spectral radiance, as calculated above, to at sensor reflectance or albedo.

This eliminates the effect of different solar zenith angles at the time of image acquisition. The combined surface and atmospheric reflectance of the Earth is achieved using the following formula (NASA, 2011):

$$\rho_\lambda = \frac{\pi L_\lambda d^2}{ESUN_\lambda \cos(\theta_s)}$$

Equation 2

Where λ is the wavelength, ρ_λ is the spectral (TOA) reflectance for wavelength λ, L_λ is the spectral radiance, d is the Earth-Sun distance in astronomical units (provided with Landsat-8 metafile), $ESUN_\lambda$ is the mean solar exoatmospheric irradiance and θ_s is the solar zenith angle in degrees, $\theta_s = 90° - \theta_e$ where θ_e is the Sun elevation. Landsat-8 images are provided with band-specific rescaling factors that allow for the direct conversion from DN to TOA reflectance. It is worth mentioning that the output reflectance, which has values 0 – 1, is multiplied by a scaling factor of 1000 so the results can be stored as a 16 bit integer.

3.1.3 Surface reflectance

TOA reflectance does not take into account the effects of scattering and absorption in the atmosphere and is simply a ratio of the at-sensor radiance with the incoming radiance from the sun. The effects of the atmosphere, the disturbance on the reflectance that varies with the wavelength, should be considered in order to measure the reflectance at the ground. As described by Moran et al., (1992), the land surface reflectance (ρ) is:

$$\rho = [\pi * (L_\lambda - L_p) * d^2] / [T_v * ((ESUN_\lambda * \cos\theta_s * T_z) + E_{down})]$$

Equation 3

Where:

L_p: the path radiance.

T_v: the atmospheric transmittance in the viewing direction.

T_z: the atmospheric transmittance in the illumination direction.

E_{down}: the down welling diffuse irradiance.

The Dark Object Subtraction (DOS) (Chavez, 1996) is a family of image-based atmospheric corrections which have proved to be preferable for precise atmospheric corrections of Landsat imagery over coastal areas (Nazeer et al., 2014).

The following assumptions are made: $T_v = 1$; $T_z = 1$; and $E_{down} = 0$ (Moran et al., 1992). On the other hand, the path radiance is:

$$L_p = M_L * DN_{min} + A_L - 0.01 * ESUN_\lambda * \cos\theta_s / (\pi * d^2)$$

Equation 4

Where:

M_L: band-specific multiplicative rescaling factor from Landsat metadata.

A_L: band-specific additive rescaling factor from Landsat metadata

DN_{min}: a digital count value for which the sum of all the pixels with digital counts lower or equal to this value is equal to the 0.01% of all the pixels from the image considered (Sobrino et al., 2004).

3.2 Geometric Correction

The process involved georeferencing the Landsat-8 image, echo-sounding bathymetries and the topographic map to the UTM/WGS84/36N. Ten ground control points evenly distributed through the area of study and well defined on the image, map and ground were collected using GPS field measurement. The ERDAS IMAGINE software has been used (Erdas, 2014), where the projection information is (Table 2):

Table 2: Projection information

UTM	Projection
Zone	36
Spheroid/Datum	WGS84
Scale factor at central meridian	0.9996
Longitude of central meridian	33°
Latitude of central meridian	0°
False easting	500,000 m
False northing	0 m

After geo-referencing (following the transformation), all data were resampled to 30 m pixel size In order to achieve a one-to-one correspondence of the water depths in the map and pixel reflectance in the image. A bilinear interpolation was used for resampling, which results in a better quality image than nearest neighborhood resampling and requires less processing than cubic convolution (Lillesand et al., 2004). The RMSE achieved for georeferencing the image and the map were 0.6 and 0.9 pixel respectively.

3.3 Ground and Water Separation

In order to estimate water depths accurately, water and ground in the image were separated. Since the near infrared bands are intensively absorbed by water and the pixels with the reflectance higher than 5% are likely to represent ground (Yanjiao et al., 2007), the masked image was built using the near infrared bands and superimposed on the Landsat-8 bands to define the ground as shown in figure 3.

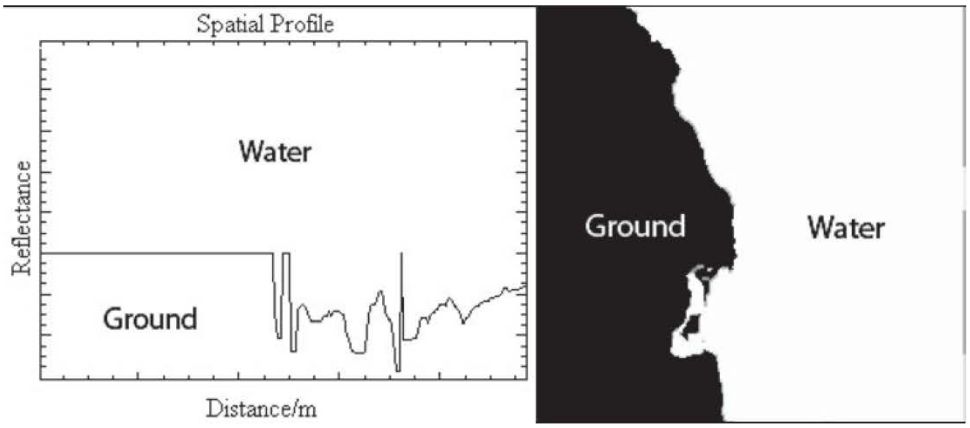

Figure 3: Reflectance variation from land to water (left); the masked pixels of land (right)

3.4 MLP-Based Probability

MLP is the most widely used type of ANN. A *MLP* is a feed-forward ANN model that maps sets of input data onto a set of appropriate outputs (Rumelhart et al., 1986). A *MLP* consists of multiple layers of nodes in a directed graph, with each layer fully connected to the next one. Except for the input nodes, each node is a neuron (or processing element) with a nonlinear activation function. *MLP* utilizes a supervised learning technique called back-propagation for training the network. Mathematically this can be written as:

$$y = \varphi(\sum_{i=1}^{n} w_i x_i + b) = \varphi(w^T x + b)$$

Equation 5

Where w denotes the vector of weights, x is the vector of inputs, b is the bias and φ is the activation function. The activation function is chosen to be the sigmoid $1/(1+e^{-x})$. This function allows *MLP* networks to model nonlinear mappings well (Cybenko, 1989).

3.5 NB-based Probability

NB is a supervised classification method derived from the Bayes theorem. It requires no complicated iterative parameter estimation. On the other hand, it requires a small amount of training data to estimate the parameters necessary for classification. Despite its simplicity, the *NB* often outperforms more sophisticated classification methods including support vector machines (Rennie et al., 2003). This makes it particularly useful for estimating water depths from optical satellite imagery (Jay and Guillaume, 2014). For training data with a continuous attribute x, the data is first segmented by class c, and then the mean μ_c and variance σ_c^2 of x in each class is computed. Then, the probability *distribution* of some value given a class, $P(x=v|c)$, can be computed as follows:

$$P(x = v|c) = \frac{1}{\sqrt{2\pi\sigma_c^2}} e^{\frac{(v-\mu_c)^2}{2\sigma_c^2}}$$

Equation 6

A value of $P(x=v|c)$ greater than 1 is acceptable since it is a probability density rather than a probability, and hence the posterior probability is given by:

$$Posterior(c) = \frac{p(c)p(x = v_1|c)p(x = v_2|c)\ldots p(x=v_n|c)}{evidence}$$

Equation 7

Where:

$$evidence = p(c_1)p(x = v_1|c_1)p(x = v_2|c_1)\ldots p(x = v_n|c_1) + p(c_2)\,p(x = v_1|c_2)p(x = v_2|c_2)\ldots p(x = v_n|c_2) + \ldots$$

Equation 8

3.6 FMV-Based Combination of NB and MLP Probability

In this research, *FMV* has been proposed to combine the probabilities obtained for *NB* and *MLP* and hence the individual advantages of each algorithm can be combined. The combined probability based on *FMV* can be calculated as (Zadeh, 1983):

$$P_{FMV} = \arg\max_{k} \left[\sum_{i=1}^{N} w_{p_i}\, pp_i \right]$$

Equation 9

Where pp_i is the class probability of pixel i, k is the number of classes and w_{p_i} is the weight based on the linguistic quantifier defined as (Yager, 1998):

$$w_{P_i} = Q_{P_i}\left(\frac{I}{N}\right) - Q_{P_i}\left(\frac{I-1}{N}\right), \text{ for } I = 1, \ldots, N$$

Equation 10

Q_{P_i} is the membership functions of relative quantifiers, I is the order of the algorithm after ranking Q_{P_i} for both algorithms in a descending order and N is the total number of algorithms. With parameters a, b ∈ [0, 1], Q_{P_i} can be defined as (Herrera and Verdegay, 1996):

$$Q_{P_i} = \begin{cases} 0 & \text{if } pp_i < a \\ \dfrac{pp_i - a}{b - a} & \text{if } a \le pp_i \le b \\ 1 & \text{if } pp_i > b \end{cases}$$

Equation 11

3.7 IPWI-Based Water Depths

The proposed *IPWI* technique is a modification of the simplest and most widely used inverse distance weighted technique. The *IPWI* estimates the value Z of a pixel P as a function of the *FMV* probabilities of the known k points in the training dataset.

In this regard, it is assumed that estimated elevations are more likely to be similar to elevations with higher probabilities than to elevations with lower ones. The lower probability a point, the less it influences the estimate, and hence the depth at unknown points can be determined as follows:

$$Z_p = \frac{\sum_{i=1}^{k}\left(\frac{z_i}{1-P_{FMV_i}}\right)}{\sum_{i=1}^{k}\left(\frac{1}{1-P_{FMV_i}}\right)}$$

Equation 12

For clarity, figure 4 shows an illustration of depth estimation of pixel p using its combination of *FMV* probabilities (40%, 30%, 5%, 5%, 10%, 5% and 5%) of seven known depths (11, 12, 4, 2, 7, 3 and 5 m) in a training dataset.

4. Results and Analysis

First, raw satellite DN values of Lansat-8 blue band were converted to radiances, figure 5. The radiances were then converted to surface reflectance, figure 5b. Seven image pixels with known depths have been used as training data that represent a variety of water depths over different bottom types as shown in figure 6.

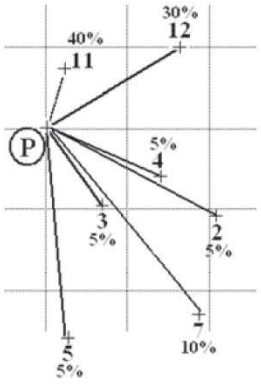

$$Zp = \frac{\frac{11}{0.6}+\frac{12}{0.7}+\frac{7}{0.9}+\frac{2}{0.95}+\frac{3}{0.95}+\frac{4}{0.95}+\frac{5}{0.95}}{\frac{1}{0.6}+\frac{1}{0.7}+\frac{1}{0.9}+\frac{1}{0.95}+\frac{1}{0.95}+\frac{1}{0.95}+\frac{1}{0.95}} = \frac{57.991}{8.417} = 6.890 \text{ m}$$

Figure 4: Depth estimation using the IPWI procedure

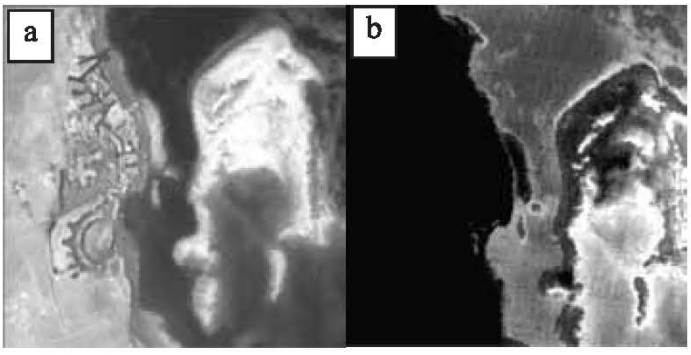

Figure 5: a) radiance; b) surface reflectance

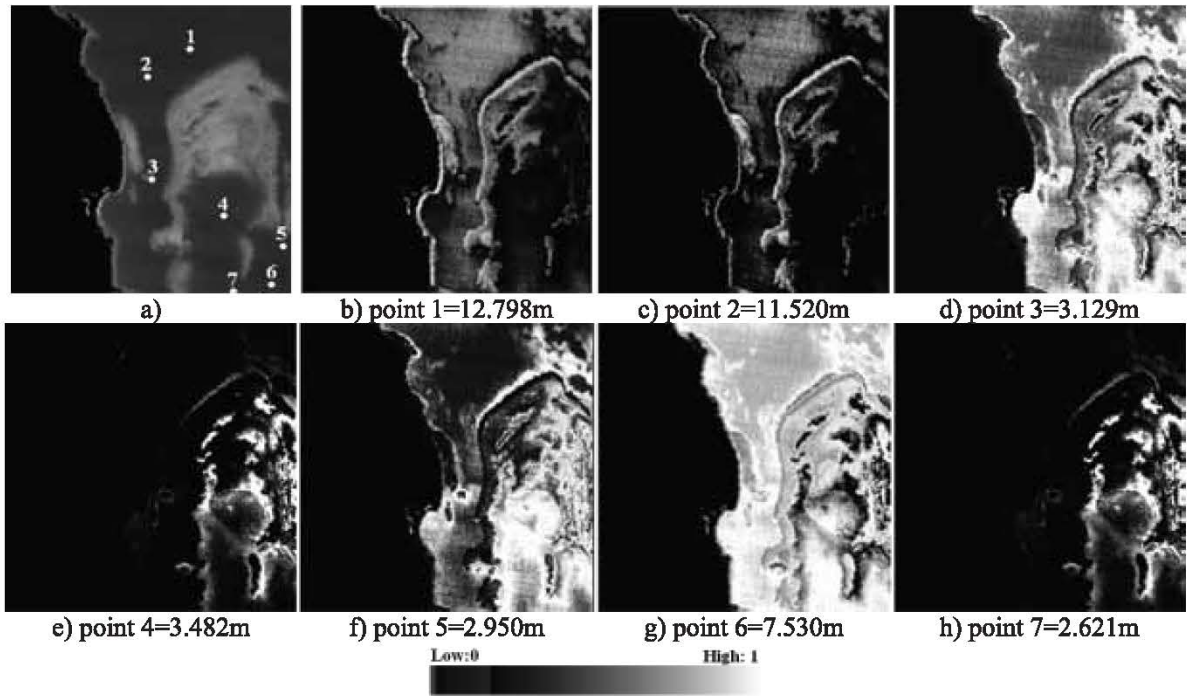

Figure 6: (a) The seven image pixels used as training data; (b) through (h) the corresponding P_{FMV} probability values

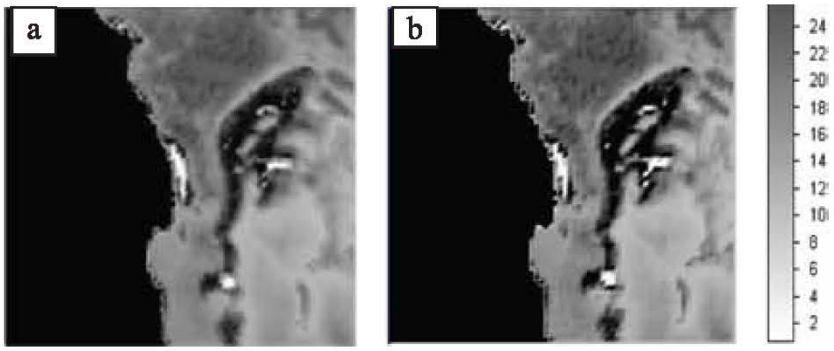

Figure 7: The water depths interpolated by: a) *IPWI*; b) *MLP*

All data points in this set were acquired using echo-sounder and multi-beam sonar platforms in November 2011. Beginning with the training dataset, Both *MLP* and *NB* algorithms were run with features of the reflectance from blue band. The structure of the *MLP* model was as follows: the numbers of input, hidden and output layer neurons were 7, 1 and 7 respectively; learning rate was 0.01; momentum factor was 0.5; sigmoid constant was 1; and number of iterations was 10000. For both *MLP* and *NB algorithms*, each pixel was classified into a combination of probability of 7 clusters. The *FMV* was then run to combine the probabilities from both classifiers with the parameter pair (0, 0.5) in equation 11. As a result, seven combined probability values have been obtained for each pixel as shown in figures 6(b) through 6(h).

The P_{FMV} values represent true probabilities in the range of 0 to 1, where 0.0 expresses absolute improbability and 1.0 expresses a complete assignment to a known depth. In order to estimate the water depths, the P_{FMV} values (images) were then presented as input data for the *IPWI*. The application of the *IPWI* resulted in a grey scale depth image as shown in figure 7(a). For comparison purposes, the traditional *MLP* were run with the same structure as above and the result is displayed in Figures 7(b). In order to evaluate the performance of the proposed method, the minimum, maximum, mean, standard deviation (SD) and the coefficient of determination (R^2) of the differences between estimated and observed water depths were determined for both *IPWI* and *MLP* and presented in table 3.

Table 3: The results of the *IPWI* method compared with *MLP*

Model	Min.	Max.	Mean	SD	R^2
MLP	1.23	6.64	1.68	0.87	0.965
IPWI	0.98	4.67	1.43	0.58	0.996

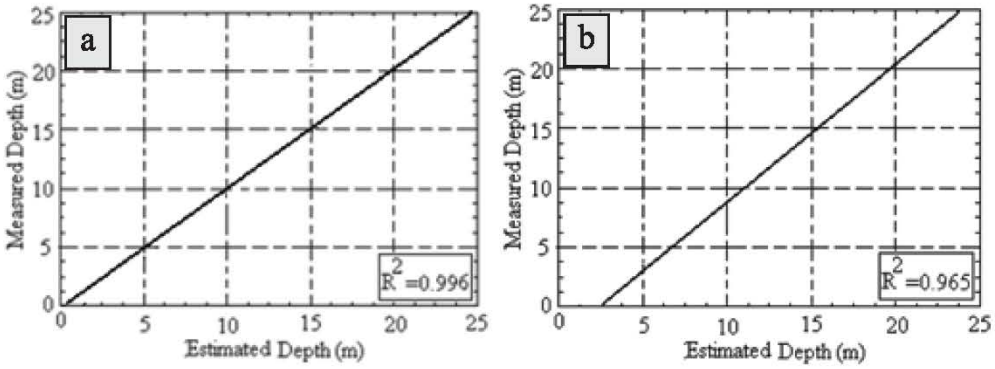

Figure 8: the graphical representation of linear correlation between measured depths with estimated depths for: (a) the *IPWI*; (b) *MLP* methods

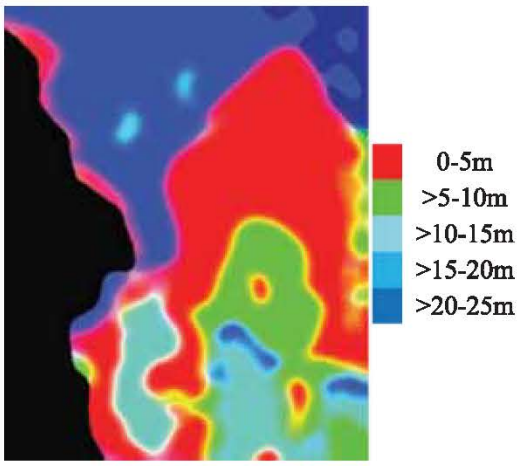

Figure 9: The results of the *IPWI* method divided as five ranges

The coefficient of determination, $0 < R^2 < 1$, accounts for how much information is shared by the reference and estimated depths (Roehl and Conrads, 2006). In the case of *IPWI*, the mean error was 1.43 m. The low standard deviation of 0.58 m indicates that the differences between estimates depths and echo sounding data are small. On the other hand, R^2 of 0.996 indicates that 99.6% of the total variation in water depths can be explained by the relationship between the reference and estimated depths. The other 0.4% of the total variation in water depths remains unexplained. Results were slightly less accurate with the *MLP*, giving a mean error of 1.68 m, SD of 0.87 m and $R^2 = 0.995$. Figure 8 shows the graphical representation of linear correlation coefficient between measured depths with estimated ones. In depths <5 m, *IPWI* method provides depth information 1–3 m deeper than the *MLP* method. Depth retrievals are possible to nearly 25 m with *IPWI* method, whereas the *MLP* fails at 23–24 m. In order to evaluate the performance of the proposed method further, the estimated depths were compared with measured depths by segmenting the depths into five 5m ranges as shown in figure 9. The results of the *IPWI* method are shown on a color scale, from red (0-5 m) to dark blue (20-25 m) with black color representing the masked land. As can be observed, figure 9 shows smooth transitions from shallow to deep water with less speckle error. Table 4 summaries an analysis of the depths obtained in the five ranges.

Table 4: analysis of the depths obtained in the five ranges

Class	Range	Counts	Min	Max	Mean	SD
Very Shallow	0-5	97	0.11	0.52	0.25	0.19
Shallow	5-10	37	0.13	0.97	0.58	0.21
Moderate	10-15	39	0.57	1.24	0.97	0.39
Deep	15-20	41	1.34	2.31	1.88	0.63
Very Deep	20-25	31	2.42	3.92	2.54	0.67

The analysis shows that the *IPWI* method enabled the water depths of less than 5 m to be estimated accurately with mean error of 0.25 m and SD of 0.19 m. Errors are slightly greater for the depths of more than 10 m. These relatively large errors could be cause by the reduction of the penetration of the solar radiation hardly in the deeper water. However, it is clear that the proposed method is able to represent the full range of the depths to 25 m. Once again, table 4 shows smooth transitions from shallow to deep water with less sensitivity to bottom type. Similar results have been reported in Pacheco (2015) from Landsat-8 imagery, at 30 m resolution. They used the water radiance of three bands: coastal aerosol; blue; and green. The results demonstrate that the linear algorithm is efficient for estimation of water depths of up to 12 m, showing a root mean square error of 0.89 m. The bathymetry obtained is more accurate for shallow depths (0 to 8 m) than for greater depths (8–12 m). Whereas the linear transform fails at 12–15 m, bathymetry retrievals are possible to almost 30 m with the ratio algorithm, but with a greater amount of noise. Finally, the comparison of the estimated depths with contours in the ESA topographic map, as shown in figure 10, is a further indication that the *IPWI* method is accurate especially at shallow depths, taking into account the data in the map is over 25 years.

5. Conclusions

In this paper, a method has been proposed to estimate water depths from Landsat-8 satellite imagery for the north part of the Red Sea in Egypt. The proposed method has no assumptions about water column parameters, which makes the method easier to use and more robust over variable bottom types. The proposed method has outperformed the conversional *MLP* method with a mean error of 1.43 m and a mean SD of 0.58 m. As well, the proposed method enabled the water depth of less than 5 m to be estimated accurately with mean absolute error of 0.25 m and SD of 0.19 m. However, the accuracy was not ideal for depths of more than 10 m, with the mean absolute errors ranging from 0.58 to 2.54 m. A very high coefficient of determination (R^2) of 0.996 was achieved between the estimated and measured depths. In conclusion, the proposed method can be applied effectively for determining water depth with less field measurements than conventional methods; and does not require knowledge of the water attenuation. In order to achieve better results in the future, more algoritms can be integrated into the system.

Acknowledgements

The author is indebted to Professor John Trinder, UNSW/Sydney/Australia, for helpful comments and edits.

References

Abileah, R., 2006, Mapping Shallow Water Depth from Satellite. ASPRS 2006 Annual Conference, Reno, Nevada, May 1-5, 2006.

Bierwirth, N., Lee, J. and Burne, V., 1993, Shallow Sea-Floor Reflectance and Water Depth Derived by Unmixing Multispectral Imagery. *Photogrammetric Engineering and Remote Sensing*, 59:331-338.

Bramante, J., Raju, D. And Min, S., 2010, Derivation of Bathymetry from Multispectral Imagery in the Highly Turbid Waters of Singapore's South Islands: A Comparative Study. Digitalglobe 8-Band Research Challenge 2010, Available From: Http://Www.Digitalglobe.Com/Downloads/8bc/8band_Challenge_TMSI.Pdf.

Ceyhun, O. and Andyalçın, A., 2010, Remote Sensing of Water Depths in Shallow Waters Via Artificial Neural Networks. Estuarine, *Coastal and Shelf Science*. 89(1): Pages 89–96.

Chavez, P. S., 1996, Image-Based Atmospheric Corrections—Revisited and Improved. *Photogrammetric Engineering and Remote Sensing*, 62(9):1025–1036.

Cybenko, G., 1989, Approximation by Superpositions of a Sigmoidal Function. *Mathematics of Control, Signals and Systems*, 2(4): 303–314.

Doxania, G., Papadopouloua, M., Lafazania, P., Pikridasb, C. and Tsakiri-Stratia, M., 2012, Shallow-Water Bathymetry Over Variable Bottom Types using Multispectral Worldview-2 Image. International Archives of the

Photogrammetry, *Remote Sensing and Spatial Information Sciences*, 39(B8), 25 August – 01 September 2012, Melbourne, Australia.

Erdas, 2014, Imagine Essentials Training Reference Manual, Atlanta, Georgia USA.

Fuxing, D. and Qian, D., 2003, A Technique for Extracting Water Depth Information From Multispectral Scanner Data in the South China Sea. *Marine Science Bulleting*, 22(3):55-60.

Herrera, F. and Verdegay, J. L., 1996. A Linguistic Decision Process in Group Decision Making. *Group Decision Negotiation*, 5, 165-176.

Hoepffner, N. and Zibordi, G., 2009, Remote Sensing of Coastal Waters. *Encyclopedia of Ocean Sciences* (2nd Ed.): 732-741.

Jay, S. and Guillaume, M., 2014, A Novel Maximum Likelihood Based Method for Mapping Depth and Water Quality From Hyperspectral Remote-Sensing Data. *Remote Sensing of Environment*, 147: 121–132.

Jiazhu, H. and Yuming, Y., 2002, Experiment of Water Depth Surveying in the Nantong Section of the Yangtze River. *Adnances in Water Science*, 13(2): 235-238.

Juanita C. S. and Ronald J. H., 1998, Coastal Bathymetry from Hyperspectral Observations of Water Radiance. *Remote Sensing of Environment*, 65:341- 352.

Kao, H., Ren, H., Lee, C., Chang, C., Yen, J. And Lin, T., 2009, Determination of Shallow Water Depth using Optical Satellite Images. *International Journal of Remote Sensing*, 30(23): 6241–6260.

Keith, D. J., Shaeffer, B. A., Lunetta, R. S., Gould, R. W., Rocha, K. and Cobb, D. J., 2014, Remote Sensing of Selected Water-Quality Indicators with the Hyperspectral Imager for the Coastal Ocean (HICO) Sensor. *International Journal of Remote Sensing*, 35(9), 2927–2962.

Lee, K. R., Kim, A. M., Olsen, R. C. and Kruse, F. A., 2011, Using Worldview-2 to Determine Bottom-Type and Bathymetry, *Proceedings SPIE Symposium On Defense and Security*, 25 - 29 April 2011, Orlando, FL.

Lillesand, T. M., Kiefer, R. W. and Chipman, J. W., 2004, Remote Sensing and Image Interpretation, John Wiley and Sons, Hoboken, NJ, USA, 2004.

Loomis, M. J., 2009, Depth Derivation from the Worldview-2 Satellite using Hyperspectral Imagery, Unpublished M.S. Thesis, Naval Postgraduate School, Monterey, CA, 2009.

Louchard, E. M., Reid, R. P., Stephens, F. C., Davis, C. O., Leathers, R. A. and Downes, T. V.,2003, Optical Remote Sensing of Benthic Habitats and Bathymetry in Coastal Environments at Lee Stocking Island, Bahamas: A Comparative Spectral Classification Approach. *Limnology and Oceanography*, 48(1): 511-521.

Lyzenga, D. R., Malinas, N. P. and Tanis, F. J., 2006, Multispectral Bathymetry using a Simple Physically Based Algorithm. *IEEE Transactions on Geoscience and Remote Sensing*, 44(8): 2251-2259.

Mallick, J., Abul Hasan, M., Alashker, Y. And Ahmed, M., 2014, Bathymetric and Geochemical Analysis of Lake Al-Saad, Abha, Kingdom of Saudi Arabia using Geoinformatics Technology. *Journal of Geographic Information System*, 6, 440-452.

Mehdi, G., Tiit, K., Abbas, E., Ali, A. And Babak, N., 2013, Remotely Sensed Empirical Modeling of Bathymetry in the Southeastern Caspian Sea, *Remote Sensing*, 5: 2746-2762.

Mgengel, V. and Spitzer, R. J., 1991, Application of Remote Sensing Data to Mapping of Shallow Sea-Floor nearby Netherlands. *International Journal of Remote Sensing*, 57(5):473 - 479.

Mohamed, H., Negm, A., Zahran, M. and Saavedra, O., 2015, Bathymetry Determination from High Resolution Satellite Imagery using Ensemble Learning Algorithms in Shallow Lakes: Case Study El-Burullus Lake. *International Journal of Environmental Science and Development*: 7(4): 295-301.

Monteys, X., Harris, P., Caloca, S. and Cahalane, C., 2015, Spatial Prediction of Coastal Bathymetry Based on Multispectral Satellite Imagery and Multibeam Data. *Remote Sensing*, 7: 13782-13806.

Moran, M., Jackson, R., Slater, P. and Teillet, P., 1992, Evaluation of Simplified Procedures for Retrieval of Land Surface Reflectance Factors from Satellite Sensor Output, *Remote Sensing of Environment*, 41, 169-184

NASA (Ed.), 2011, Landsat 7 Science Data Users Handbook Landsat Project Science Office At NASA's Goddard Space Flight Center In Greenbelt, Http://Landsathandbook.Gsfc.Nasa.Gov/Pdfs/Landsat7_Handbook.Pdf

Nazeer, M., Nichols, J. E. and Yung, Y., 2014, Evaluation of Atmospheric Correction Models and Landsat Surface Reflectance Product in an Urban Coastal Environment. *International Journal of Remote Sensing*, 35(16):6271–6291.

Pacheco, A., Horta, J., Loureiro, C. and Ferreira, Ó., 2015, Retrieval of Nearshore Bathymetry from Landsat 8 Images: A Tool for Coastal Monitoring in Shallow Waters. *Remote Sensing of Environment*, 159: 102–116.

Pattanaik, A., Sahu, K. And Bhutiyani, M, 2015, Estimation of Shallow Water Bathymetry using IRS-Multispectral Imagery of Odisha Coast, India. *International Conference on Water Resources, Coastal and Ocean Engineering (ICWRCOE 2015)*, Aquatic Procedia: 4(2015): 173 – 181.

Piotrowski, C. C. and Dugan, J. P., 2002, Accuracy of Bathymetry and Current Retrievals from Airborne Optical Time-Series Imaging of Shoaling Waves. *IEEE Transactions on Geoscience and Remote Sensing*, 40(12).

Puetz, A. M., Lee, K. and Olsen, R. C., 2009, Worldview-2 Data Simulation and Analysis Results, *Proceedings of SPIE*, Vol. 7334, 73340U.

Rennie, J., Shih, L., Teevan, J. and Karger, D., 2003, Tackling the Poor Assumptions of Naive Bayes Classifiers (PDF). ICML.

Roehl, E. and Conrads, P., 2006, Estimating Water Depths using Artificial Neural Networks. *7th International Conference on Hydroinformatics*, HIC 2006, Nice, France.

Rumelhart, D., Geoffrey, E. and Robert, J., 1986, Learning Internal Representations by Error Propagation, Rumelhart, D.E. And J.L. Mcclelland (Eds.), *Parallel Distributed Processing*, 1: 318-362, MIT Press, Cambridge.

Sobrino, J., Jiménez Muñoz, J. C. And Paolini, L., 2004, Land Surface Temperature Retrieval from LANDSAT TM 5, *Remote Sensing of Environment*, 90: 434-440

Stumpf, R. P., Holderied, K. and Sinclair, M., 2003, Determination of Water Depth with High–Resolution Satellite Imagery Over Variable Bottom Types. *Limnology and Oceanography*, 48: 547–556.

Su, H., Liu, H. and Heyman, W., 2008, Automated Derivation for Bathymetric Information for Multispectral Satellite Imagery using A Non-Linear Inversion Model, *Marine Geodesy*, 31: 281-298.

Tang, K. and Pradhan, B., 2015, Converting Digital Number into Bathymetric Depth: A Case Study over Coastal and Shallow Water of Langkawi Island, Malaysia. *FIG Working Week 2015, From the Wisdom of the Ages to the Challenges of the Modern World*, Sofia, Bulgaria, 17-21 May 2015.

Yager, R. R., 1988, On Ordered Weighted Averaging Aggregation Operators in Multicriteria Decision Making. IEEE Transactions on Systems, Man, and Cybernetics, 18, 183-190.

Yanjiao, W., Peiqun, Z, Wenjie, D. And Ying, Z., 2007, Study on Remote Sensing of Water Depths Based on BP Artificial Neural Network, *Marine Science Bulletin*, 9(1): 26-35.

Yuzugullu, O. And Aksoy, A., 2014, Generation of the Bathymetry of a Eutrophic Shallow Lake using Worldview-2 Imagery. *Journal of Hydroinformatics*, 16 (1): 50-59.

Zadeh, L. A., 1983, A Computational Approach to Fuzzy Quantifiers Ini Natural Languages, Computers and Mathematics with Applications, 9: 149-184.